Area-Preservation Mapping using Optimal Mass Transport

Xin Zhao, Zhengyu Su, Xianfeng David Gu, Arie Kaufman, Fellow, IEEE, Jian Sun, Jie Gao, and Feng Luo

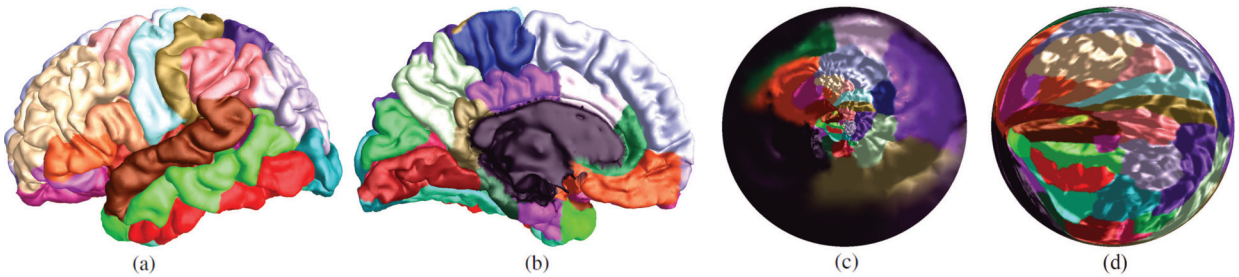

Fig. 1. Surface flattening and area manipulation using a brain surface model. A brain surface extracted from MRI data with color coded components with (a) a lateral view and (b) a medial view. The major brain folds are color coded for easy recognition. (c) Conformal mapping result, and (d) our area-preservation mapping result. By comparison, our method accurately preserves the size of the area for each fold component, while conformal mapping leads to severe area distortions (severely shrinking some brain folds while enlarging others).

Abstract—We present a novel area-preservation mapping/flattening method using the optimal mass transport technique, based on the Monge-Brenier theory. Our optimal transport map approach is rigorous and solid in theory, efficient and parallel in computation, yet general for various applications. By comparison with the conventional Monge-Kantorovich approach, our method reduces the number of variables from $O(n^2)$ to $O(n)$, and converts the optimal mass transport problem to a convex optimization problem, which can now be efficiently carried out by Newton's method. Furthermore, our framework includes the area weighting strategy that enables users to completely control and adjust the size of areas everywhere in an accurate and quantitative way. Our method significantly reduces the complexity of the problem, and improves the efficiency, flexibility and scalability during visualization. Our framework, by combining conformal mapping and optimal mass transport mapping, serves as a powerful tool for a broad range of applications in visualization and graphics, especially for medical imaging. We provide a variety of experimental results to demonstrate the efficiency, robustness and efficacy of our novel framework.

Index Terms—Area-preservation mapping, surface flattening, optimal transport map, Monge-Brenier theory, visualization and graphics applications

1 Introduction

1.1 Motivation

With the fast generation of large and complex data nowadays, it is desirable to develop new frameworks aiming at generating a visualization of the entire data needed for navigation, detection, exploration and a global understanding of selected objects or regions of interest (ROIs). Complex geometric structures are often better visualized and analyzed by mapping the surface properties, such as normal map, angle, or area, to a simple canonical domain, such as a rectangle or a sphere. Surface flattening and texture mapping offer a good way of visualizing a surface section by enabling the visualization of all surface parts within a single planar image.

In general, surface flattening and texture mapping unavoidably introduces distortions. There are two types of distortions, angle distortion and area distortion. A mapping, which is both angle preservation and area preservation, must be isometric. Therefore, the surface must have zero Gaussian curvature everywhere, namely a developable surface or a ruled surface. For general surfaces, one can only choose either angle-preservation mapping or area-preservation mapping, but never both of them simultaneously.

Angle-preservation (conformal) mapping/surface flattening preserves local shapes, and thus has been broadly used in many feature oriented applications in visualization and medical imaging. However, a conformal method usually substantially distorts area, thus failing to display accurate size of area, including height, width, thickness or diameter of ROIs. Unfortunately, these distorted area parameters are extremely important in many medical image recognition and auto diagnosis applications, such as brain fold detection [10] or colon polyps detection and diagnosis [15, 30]. Moreover, it is well known that conformal mapping induces severe area distortions for surfaces with long tube shapes, such as the elongated lion head model, as shown in Fig. 2. This disadvantage derives from the fundamental obstacle of conformal mapping theory and we can not easily overcome it. Imagine a cylinder $\mathbf{r}(\theta,z)=(\cos\theta,\sin\theta,z)$, a conformal mapping $\phi(\theta,z)=e^{-z}(\cos\theta,\sin\theta)$ maps it to the unit disk, the area distortion factor e^{-2z} is exponential with respect to the height z, and in practice easily exceeds the machine precision.

By comparison, area-preservation mapping can generate accurate and information lossless mapping results, which is a key objective for many medical imaging applications, with the ability to carry out measurements for detecting anatomic abnormalities. For example, in

- *Xin Zhao is with Computer Science Department, Stony Brook University. E-mail: xinzhao@cs.stonybrook.edu*
- *Zhengyu Su is with Computer Science Department, Stony Brook University. E-mail: zhsu@cs.stonybrook.edu*
- *Xianfeng David Gu is with Computer Science Department, Stony Brook University. E-mail: gu@cs.stonybrook.edu*
- *Arie Kaufman is with Computer Science Department, Stony Brook University. E-mail: ari@cs.stonybrook.edu*
- *Jie Gao is with Computer Science Department, Stony Brook University. E-mail: jgao@cs.stonybrook.edu*
- *Jian Sun is with Mathematics Science Center, Tsinghua University. E-mail: sunjian0813@gmail.com*
- *Feng Luo is with Mathematics Department, Rutgers University. E-mail: fluo@math.rutgers.edu*

Manuscript received 31 March 2013; accepted 1 August 2013; posted online 13 October 2013; mailed on 4 October 2013.
For information on obtaining reprints of this article, please send e-mail to: tvcg@computer.org.

virtual colonoscopy, the physician may want to measure and compare different sizes of polyps, in order to determine disease conditions and cancer risks [13]. A special case of this problem also occurs in any application where volume or area measurement is critical (e.g., brain data [10, 12, 37]). From human cognition perspective, area-preservation mapping and flattening can also enhance the viewer's ability to easily recognize the component-aware patches or long branch parts distribution of models, and consequently understand the local feature with the knowledge of a global structure (Fig. 2). Therefore, area-preservation mapping has vast potentials for many visualization and graphics applications.

To simultaneously tackle the above challenges, we have developed a flattening framework which provides a global view of the surface with minimal area distortion, while, at the same time, maximally preserving local angle/shape features on the flattened surface. In this work, we introduce our flattening framework using optimal mass transport (OMT), based on Monge-Brenier theory [6].

1.2 Optimal Mass Transport

Our approach is inspired by the similarity between our mapping problem and the OMT problem. Monge [22] has raised the classical OMT problem that concerns determining the optimal way, with minimal transportation cost, to move a pile of soil from one place to another. Formally, spaces X and Y are with measures μ and ν, respectively, the transportation cost for moving from $x \in X$ to $y \in Y$ is $c(x,y)$. The optimal transport map $T : X \to Y$ is measure preserving, namely for any $B \subset Y$, $\nu(B) = \mu(T^{-1}(B))$, it minimizes the total transportation cost $\int_X c(x,T(x))\mu(x)dx$. From OMT perspective, the surface mapping/flattening can be viewed as an optimal transport map T, and the size of area can be viewed as the preserved measures μ and ν.

The solution of the OMT problem lies at the following theory. Kantorovich [16] has proved the existence and uniqueness of the optimal transport plan. The Monge-Kantorovich optimization is as follows, the space X and Y are discretized to samples $X = \{x_1, x_2, \cdots, x_n\}$, $Y = \{y_1, y_2, \cdots, y_n\}$, with Dirac measures $\mu = \{\mu_i\}$, $\nu = \{\nu_j\}$. A transport plan is represented as n^2 unknown variables γ_{ij}, $\sum_i \gamma_{ij} = \sum_j \gamma_{ij} = 1$, γ_{ij} represents the percentage of μ_i at x_i, which is transported to y_j. Then the total transportation cost is a linear function $\sum_{ij} \gamma_{ij} c(x_i, y_j)$. Thus the optimal transport plan can be solved using a linear programming method on n^2 variables.

Monge-Kantorovich optimization has been used in numerous fields from physics, econometrics to computer science, including data compression and image processing [23]. Recently, researchers have realized that optimal transport could provide a powerful tool in image processing, if one could reduce its high computational cost [10, 27]. However, it has one fundamental disadvantage that the number of variables is $O(n^2)$, which is unacceptable to visualization and graphics applications since a high resolution 3D/volume dataset normally includes more than 10^6 vertices.

An alternative Monge-Brenier optimization can significantly reduce the number of variables. Brenier [7] has developed a different approach for special optimal transport problem, where the cost function $c(x,y)$ is a quadratic distance $c(x,y) = \|x-y\|^2$. Brenier's theory proves that there is a convex function $u : X \to \mathbb{R}$, and the unique optimal transport map is given by its gradient map, $x \to gradu(x)$. The Monge-Brenier's approach reduces the unknown variables from n^2 to n, which greatly reduces the computational cost, and improves the efficiency. In our framework, we follow Monge-Brenier's approach.

1.3 Area-Preservation Mapping/Flattening

Texture mapping on arbitrary surfaces with minimal distortion can preserve the local and global structure of the texture [36]. Dominitz and Tannanbaum [10] have proposed a method to compose conformal mapping with an area-preservation mapping, using the technique of OMT, based on Monge-Kantorovich theory [16], which accurately preserves the area element and also maximally preserves the angle. Suppose we want to compute an area-preservation map from a metric surface $(S, \mathbf{g})$, where $\mathbf{g}$ is the Riemannian metric, to the planar disk $\mathbb{D}$.

Fig. 2. Disadvantages of conformal mapping for elongated shapes. (a) Front view and (b) back view of the elongated lion head surface model. Surface flattening results induced by (c) conformal mapping and by (d) our area-preservation mapping. Conformal mapping generates major area distortions for both the lion face and the vase regions, while our method preserves them accurately for clear view without losing any information (highlighted by the red circles).

The method starts with an angle preserving $\phi : S \to \mathbb{D}$, which introduces area distortions on the disk; the area distortion factor is used to define a measure on the disk, denoted as μ. Then, an optimal mass transport map is computed between the disk with this measure and the disk with the Euclidean measure $dxdy$, $\psi : (\mathbb{D}, \mu) \to (\mathbb{D}, dxdy)$. The composition $\psi \circ \phi : S \to \mathbb{D}$ gives the area-preservation map.

Their method is based on Monge-Kantorovich's theory and approaches, which require n^2 variables. For example, in image registration applications, a 1024×1024 image would result in 2^{40} variables, the storage cost is thus very high, and the computation is extremely expensive.

In contrast, we use Monge-Brenier's approach to compute the optimal transport map. Our discrete algorithm is solidly based on the variational principle [11]. Basically, we only discretize the target space Y, and find a convex function whose gradient gives the optimal transport map. Finding the OMT is equivalent to optimizing a convex energy, which can be efficiently achieved using Newton's method. The whole computation requires only n variables. Therefore, this method greatly reduces the computation cost and improves the efficiency.

Our Contributions

The key contribution of this work is the introduction of a novel area-preservation mapping/flattening algorithm using the optimal transport technique, based on Monge-Brenier theory. The new method has the following merits:

- It reduces the number of variables from n^2 to n, greatly reducing the complexity.
- It converts the optimal mass transport problem to a convex optimization problem, and can be solved using Newton's method, greatly improving the efficiency.
- The algorithm gives users full control of the size of area everywhere. Users can design and manipulate the area of each triangular component freely, improving the flexibility.

The organization of this paper is as follows: In Section 2, we review and discuss related work. In Section 3 and Section 4, we describe the theory of our OMT optimization and sketch the analytical procedure and algorithms to find the optimal mapping. We illustrate examples using our framework, discuss relevant implementation issues and present distortion comparisons in Section 5. Finally, in Section 6, we summarize our work as conclusion and propose some possible future research directions.

2 Related Work

We review the research projects on optimal mass transport that are most relevant to our approach targeting both algorithms and applications, and discuss the comparisons with our framework.

Theoretic Development. In 1781, Monge [22] has formulated the OMT problem. In the 1940's, Kantorovich [16] has proved the existence and the uniqueness of the optimal transport plan. At the end of 1980's, Briener [7] has proved that the optimal transport map is the gradient map of a convex function, when the transportation cost is the quadratic of the Euclidean distance. In the discrete case, Brenier's result is equivalent to the existence and the uniqueness of the convex polyhedron with prescribed projected facet areas. This has been first shown by Alexandroff [3] in 1920's. Aurenhammer [4] has shown the connection between Brenier's construction and power diagram, where the existence has been proven. Recently, the connection between the discrete optimal transport map and the discrete Monge-Ampere equation, which is based on variational approach, has been given by Gu et al. [11].

Monge-Kantorovich Approach. Most existing works are based on Monge-Kantorovich approach. Bonnel et al. [5] have proposed a method for interpolation between distributions or functions based on advection instead of blending for rendering purposes. This method decomposes distributions or functions into sums of radial basis functions (RBFs), then solves a mass transport problem to pair the RBFs and applies partial transport to obtain the interpolated function. Rubner et al. [25] have proposed a content based image retrieval method using the earth mover distance as a metric for the OMT problem. However, it fails to give a warped grid, an essential requirement for image registration and image morphing. Rehman et al. [27] have listed several advantages of the OMT method for multiresolution 2D/3D nonrigid registration. Meanwhile, they stress the fact that the optimization of OMT is computationally expensive and emphasize that it is important to find efficient numerical methods to solve this issue.

Monge-Brenier's Approach. The following techniques are based on Monge-Brenier's approach. Merigot [21] has proposed a multiscale approach to solve the optimal transport problem. To solve an optimal transport problem between a measure with density μ to a discrete measure ν, this method builds a sequence $\nu_0 = \nu, \ldots, \nu_L$ of simplifications. Then, it first solves the easier transport problem between μ and ν_L, and uses the solution of the problem to be the initial guess for the optimal transport between μ and $\nu_{(L-1)}$. This step is iterated until a solution to the original OMT problem. The method is applied for computing the Wasserstein distances between probability distributions, and for image interpolation. de Goes et al. [9] have provided an optimal transport driven approach for 2D shape reconstruction and simplification. They have further presented a formulation of capacity constrained Voronoi tessellation as an optimal transport problem for image processing [8]. This method produces high quality blue noise point sets with improved spectral and spatial properties. Compared to our method, de Goes's method only applies between 2D domains while our method maps a 3D surface to a 2D domain. Our method can further lead to a fast, scalable algorithm to generate high quality blue noise point distributions of arbitrary density functions.

Minimal Flow Method. Tannenbaum group has introduced this novel approach. The basic idea is to construct an initial mass preservation mapping, then deform the mapping such that the total transportation cost is reduced and the deformed mapping is still mass preserving. Namely, it designs a gradient flow in the space of all mass preservation mapping space. Haker et al. [14] have presented a method for image registration and warping based on the OMT. The method is parameter free and has the unique global optimum. However, its linear programming of the optimal map can be solved with $O(n^2)$ variables, which is prohibitively expensive when n is large. Zhu et al. [34] have combined conformal mapping and area-preservation mapping for flattening branched physiological surfaces, such as vessels. The optimal transport map is carried using the minimal flow approach. Similar method has been applied for image morphing [35]. Rehman et al. [27] have applied the minimizing flow approach for the OMT with applications to non-rigid 3D image registration. The implementation also employs multi-grid and parallel methodologies on a consumer graphics processing unit (GPU) for fast computation. Although computing the optimal map has been shown to be computationally expensive in the past, we show that our approach is orders of magnitude faster than previous work. Dominitz and Tannenbaum [10] have proposed to use the OMT for texture mapping. The method begins with an angle-preservation mapping and then corrects it using the mass transport procedure derived via a certain gradient flow. A multiresolution scheme is incorporated into the flow to obtain fast convergence to the optimal mapping. Both methods require designing divergence free vector fields to drive a diffeomorphic flow to minimize the energy.

Comparison. Our method mainly follows the Monge-Brenier approach, based on the variational principle [11]. Comparing to the state-of-the-art techniques, it has many merits as follows:

- Comparing to the Monge-Kantorovich approaches [5, 16, 27], our method only requires $O(n)$ variables. In contrast, Kantorovich approach requires $O(n^2)$ variables. Therefore, our method greatly reduces the storage complexity, and it is thus much more efficient.
- Comparing to the Monge-Brenier based approaches [8, 9, 21], all the existing methods are for image processing tasks. Our method however focuses on surfaces. For image processing, the samples are relatively uniform, and therefore, the computation is relatively stable. In our case, the sample points are produced by the conformal mapping, the sample density is highly non-uniform, and thus conventional methods are very vulnerable and error-prone for the large area distortions induced by the conformal mapping. Our experiments indicate that conventional methods are not robust enough. Therefore, we have specially designed our *step length control* algorithm (Section 4.2) to improve the robustness.
- Comparing to the minizing flow methods [10, 14, 35], the solution of latter is equivalent to a gradient descend method for optimizing the transportation cost. In contrast, our method is equivalent to the Newton's method to optimize a convex energy, which has a higher order convergence rate. Therefore, our method is more efficient.

3 Theoretical Foundation

In this section, we present the theoretical foundation of our framework.

3.1 Optimal Mass Transport

Monge's Problem. The problem of finding a map T minimizing Eqn. 1 (such that $\nu = T_{\#}\mu$), has been first studied by Monge [6] in the 18th century. Let X and Y be two metric spaces with probability measures (volumes or areas) μ and ν, respectively. Assume X and Y have equal total measures (volumes or areas):

$$\int_X \mu = \int_Y \nu.$$

A map $T : X \to Y$ is *measure preserving* (volume or area preservation) if for any measurable set $B \subset Y$, such that:

$$\mu(T^{-1}(B)) = \nu(B).$$

Let us denote by $c(x,y)$ the transportation cost for sending $x \in X$ to $y \in Y$, then, the total *transportation cost* is given by:

$$\int_X c(x,T(x))d\mu(x). \tag{1}$$

If this condition is satisfied, ν is said to be the push forward of μ by T, and we write $\nu = T_{\#}\mu$.

In the 1940s, Kantorovich [16] has introduced the relaxation of Monge's problem and solved it using linear programming. At the end of 1980's, Brenier [7] has proved that there is a convex function $f : X \to \mathbb{R}$, and the optimal mass transport map is given by the gradient map $x \to \nabla f(x)$.

3.2 Discrete Optimal Mass Transport

Suppose μ has compact support on X, define:

$$\Omega = supp\ \mu = \{x \in X | \mu(x) > 0\},$$

and assume Ω is a convex domain in X. The space Y is discretized to $Y = \{y_1, y_2, \cdots, y_n\}$ with Dirac measure $\nu = \sum_{j=1}^{n} \nu_j \delta(y - y_j)$.

We define a *height vector* $\mathbf{h} = (h_1, h_2, \cdots, h_n) \in \mathbb{R}^n$, consisting of n real numbers. For each $y_i \in Y$, we construct a hyperplane defined on X:

$$\pi_i(\mathbf{h}) : \langle x, y_i \rangle + h_i = 0, \tag{2}$$

where $\langle , \rangle$ is the inner product in $\mathbb{R}^n$.

Define a function:

$$u_{\mathbf{h}}(x) = \max_{1 \le i \le n} \{\langle x, y_i \rangle + h_i\}, \tag{3}$$

then $f(\mathbf{h}, x)$ is a convex function. We denote its graph by $G(\mathbf{h})$, which is an infinite convex polyhedron with supporting planes $\pi_i(\mathbf{h})$. The projection of $G(\mathbf{h})$ induces a polygonal partition of Ω,

$$\Omega = \bigcup_{i=1}^{n} W_i(\mathbf{h}), W_i(\mathbf{h}) = \{x \in X | u_{\mathbf{h}}(x) = \langle x, y_i \rangle + h_i\} \cap \Omega. \tag{4}$$

Each cell $W_i(\mathbf{h})$ is the projection of a facet of the convex polyhedron $G(\mathbf{h})$ onto Ω. The convex function $u_{\mathbf{h}}$ on each cell $W_i(\mathbf{h})$ is a linear function $\pi_i(\mathbf{h})$, therefore, the gradient map

$$grad\ u_{\mathbf{h}} : W_i(\mathbf{h}) \to y_i, i = 1, 2, \cdots, n. \tag{5}$$

maps each $W_i(\mathbf{h})$ to a single point y_i.

The following theorem plays a fundamental role here:

Theorem 1 *For any given measure ν, such that*

$$\sum_{j=1}^{n} \nu_j = \int_\Omega \mu, \nu_j > 0,$$

there must exists a height vector $\mathbf{h}$ *unique up to adding a constant vector $(c, c, \cdots, c)$, the convex function Eqn. 3 induces the cell decomposition of Ω, Eqn. 4, such that the following* area-preservation constraints *are satisfied for all cells,*

$$\int_{W_i(\mathbf{h})} = \nu_i, i = 1, 2, \cdots, n. \tag{6}$$

Furthermore, the gradient map $gradu_{\mathbf{h}}$ optimizes the following transportation cost

$$E(T) := \int_\Omega |x - T(x)|^2 \mu(x) dx. \tag{7}$$

The existence and uniqueness have been first proven by Alexandrov [3] using a topological method. The existence has been also proven by Argmstrong [4], and the uniqueness and optimality have been proven by Brenier [7].

Recently, Gu et al. [11] have given a novel proof for the existence and uniqueness based on variational principle. We follow their approach in our paper. First, define the admissible space of the height vectors:

$$H_0 := \{\mathbf{h} | \int_{W_i(\mathbf{h})} \mu > 0, \sum_i h_i = 0\}.$$

Then, define the energy $E(\mathbf{h})$ as the volume of the convex polyhedron bounded by the graph $G(\mathbf{h})$ and the cylinder through Ω minus a linear term,

$$E(\mathbf{h}) = \int_\Omega u_{\mathbf{h}}(x)\mu(x)dx - \sum_{i=1}^{n} \nu_i h_i. \tag{8}$$

The gradient of the energy is given by:

$$\nabla E(\mathbf{h}) = \left(\int_{W_i(\mathbf{h})} \mu - \mu_i \right), \tag{9}$$

Suppose the cells $W_i(\mathbf{h})$ and $W_j(\mathbf{h})$ intersects at an edge $e_{ij} = W_i(\mathbf{h}) \cap W_j(\mathbf{h}) \cap \Omega$, then, the Hessian of $E(\mathbf{h})$ is given by:

$$\frac{\partial^2 E(\mathbf{h})}{\partial h_i \partial h_j} = \begin{cases} \int_{e_{ij}} \mu & W_i(\mathbf{h}) \cap W_j(\mathbf{h}) \cap \Omega \neq \emptyset \\ 0 & otherwise \end{cases} \tag{10}$$

In Gu et al. [11], it is proven that H_0 is convex, and the Hessian is positive definite on H_0, this implies the convexity of the energy in Eqn. 8. Furthermore, the global unique minimum $\mathbf{h}$ is an interior point of H_0. At the minimum point, $\nabla E(\mathbf{h}) = 0$, this implies the gradient map $gradu_{\mathbf{h}}$ meets the measure-preserving constraints in Eqn. 6. Furthermore, this gradient map is the optimal mass transportation map.

Due to the convexity of the volume energy (Eqn. 8), the global minimum can be obtained efficiently using Newton's method. Comparing to Kantorovich's approach, where there are n^2 unknowns, this approach has only n unknowns.

3.3 Conformal Mapping

In our current work, we also apply conformal mapping [29] to map a topological surface onto the planar domain. Suppose $(S, \mathbf{g})$ is a surface embedded in $\mathbb{R}^3$, with the induced Euclidean metric $\mathbf{g}$. Let the mapping $\phi : (S, \mathbf{g}) \to (\mathbb{D}, dx^2 + dy^2)$ transform the surface to the planar unit disk $\mathbb{D}$, where $dx^2 + dy^2$ is the planar Euclidean metric. We say ϕ is a conformal mapping, or angle-preservation mapping, if ϕ is a diffeomorphism, such that:

$$g(x,y) = e^{2\lambda(x,y)}(dx^2 + dy^2),$$

where $\lambda : S \to \mathbb{R}$ is a smooth function defined on the surface, the so called *conformal factor*.

Theorem 2 (Riemann Mapping) *Suppose $(S, \mathbf{g})$ is an oriented metric surface, which is of genus zero with a single boundary. Given an interior point $p \in S$ and a boundary point $q \in \partial S$, there is a unique conformal mapping $\phi : S \to \mathbb{D}$, satisfying $\phi(p) = 0$ and $\phi(q) = 1$.*

We follow the approach proposed by Dominitz et al. in [10], which gives us an area-preservation mapping with shape preservation. First, we map the surface $(S, \mathbf{g})$ onto the planar disk using a Riemann mapping $\phi : S \to \mathbb{D}$, then the conformal factor defines a measure on $\mathbb{D}$, $e^{2\lambda(x,y)}dxdy$. We construct an optimal mass transport map $\tau : (\mathbb{D}, e^{2\lambda(x,y)}dxdy) \to (\Omega, dxdy)$, where Ω is a planar convex domain, the composition $\tau \circ \phi : (S, \mathbf{g}) \to (\Omega, dxdy)$ is an area-preservation mapping.

4 Optimal Mass Transport Map

This section gives the detailed algorithms for the optimal mass transport map generation. Fig. 3 shows the pipeline of our OMT based area-preservation framework. The input surface is approximated by a triangular mesh M, with vertex sets V, face sets F and a convex planar domain Ω, represented as a convex polygon. Our goal is to compute an area-preservation map from the mesh M to the planar domain Ω.

Our discrete algorithm is based on the Monge-Briener theory and utilizes the variational principle to solve the optimization problem. For the input, aiming to get ROIs with arbitrary shape (e.g., irregular shape of the brain folds), we utilize the saliency map [18] for the ROI detection. Once users specify local area weight $\overline{w_i}$ everywhere, the system will iteratively solve the OMT map and refine the area-preservation result that yields strict equality of weighted sizes of area between the input surface and flattened plane. The area weighting parameter $\overline{w_i}$ is defined as weighted areas in 2D or weighted volumes in 3D. After the generation of the OMT map (bijectively area-preservation mapping), we directly apply the ROI guided texture mapping to obtain the output.

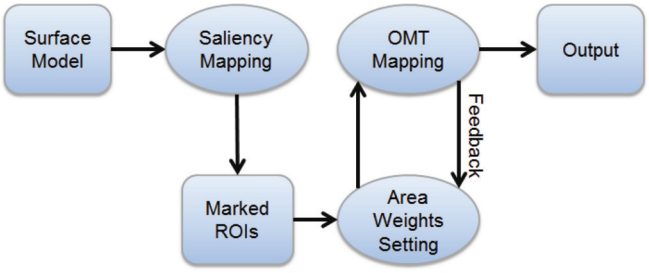

Fig. 3. The pipeline of our OMT based area-preservation framework.

Merits of Saliency Map. The application of saliency map can (1) accurately detect arbitrary ROI shape to obtain the accurate area preservation; and (2) provide hierarchical resolution of surface models, supporting the reduction of triangles in the context area, while preserving high resolution ones in ROIs, for the purpose of fast computation. Take the brain model as an example, instead of using the original model with 100K faces, with the saliency guided ROI detection, we can significantly reduce the face account to 10K or less (data oriented).

4.1 Initialization

Our algorithm uses the conformal mapping result (angle preservation) to set up the initial position for each vertex v_i. We first normalize the mesh such that its total area equals to the area of the planar domain Ω. We then initialize a discrete conformal mapping $\phi : M \to \mathbb{D}$. In our framework, we utilize the discrete Ricci flow method [29] to achieve this step. Then, after assigning each vertex a target area $\bar{w}_i$, we define for each vertex $v_i \in V$ the Dirac measure associated with it, as one third of the total area of faces adjacent to it,

$$\mu(v_i) = \frac{1}{3} \sum_{[v_i,v_j,v_k] \in F} Area([v_i,v_j,v_k]),$$

where $[v_i,v_j,v_k]$ represents the triangle formed by vertices v_i, v_j and v_k.

We use the images of all the vertices as the sample points of the unit disk $\mathbb{D}$, $Y = \{\phi(v_i) | v_i \in V\}$, each sample $\phi(v_i)$ is associated with the Dirac measure $\mu(v_i)$. By translation and scaling, we transform Y to be contained by Ω.

4.2 Optimal Mass Transport Mapping

According to the Monge-Briener theory, we need to find the height vector $\mathbf{h} = (h_1, h_2, \cdots, h_n)$. Fix a height vector, the support planes are given by $\pi_i(\mathbf{h}) : \langle x, y_i \rangle + h_i$, the convex function is $u_{\mathbf{h}}(x) = \max_i \langle x, y_i \rangle + h_i$, and its graph $G(\mathbf{h})$ can be computed as upper envelope of the supporting plane $\pi_i(\mathbf{h})$. The projection of $G(\mathbf{h})$ onto Ω forms a polygonal partition $\Omega = \bigcup_i W_i(\mathbf{h})$.

The implementation details are listed in Alg. 1. In order to preserve the area of cell W_i, we need to iteratively update the virtual variable for each vertex with height vector $\mathbf{h} = (h_1, h_2, \cdots, h_n)$ (details in the paragraph Initial Height Vector below). Thus, in each iteration, we first compute the power diagram, using each vertex as a point and the weighted radius as the power in the diagram. Then, in step 3, we compute the dual triangulation of this calculated power diagram (details in the paragraph Power Diagram below). We record every edge length in both the power diagram and its dual triangulation in this step to form the Hessian matrix. In step 4 (the last step of each iteration), we use Newton's method to solve the gradient energy equation (Eqn. 9) and to update the height vector $\mathbf{h}$ until it satisfies that $\|w_i - \overline{w_i}\|$ of each cell is less than δw (details in the paragraph Hessian Matrix below). Finally, in step 6, we update the vertex position as the center of the power Voronoi diagram to obtain the parameterization result with area-preservation.

Algorithm 1 Area-preservation Mapping

Input: Input triangular mesh M, total area π and area difference threshold δw.

Output: A unique diffeomorphic area-preservation mapping $f : M \to \mathbb{D}$, where $\mathbb{D}$ is a unit disk. The area w_i of each cell $W_i \in \mathbb{D}$ is close to the target area $\overline{w_i}$.

1. Run conformal mapping by discrete Ricci flow method [29] $\phi : M \to \mathbb{D}$, where $\mathbb{D}$ is a unit disk. Assign each site $\phi(v_i) \in \mathbb{D}$ with zero power weight, and target area $\overline{w_i} = \mu(v_i)$ defined above. Translate and scale all sites so that they are in the unit disk.
2. Compute the power diagram and calculate the area w_i of each cell W_i.
3. Compute the dual power Delaunay triangulation, and compute the lengths of edges in the diagram and triangulation to form the Hessian matrix of the convex energy in Eqn. 7 .
4. Update the power $\mathbf{h} \leftarrow \mathbf{h} + H^{-1}(\bar{\mathbf{w}} - \mathbf{w})$.
5. Repeat step 2 through step 4, until $\|w_i - \overline{w_i}\|$ of each cell is less than δw.
6. Compute the centroid of cell W_i, denoted as c_i. Then the area-preservation mapping is given by $\tau^{-1} \circ \phi(v_i) = c_i$, where τ is the Brénier map $\tau : W_i \to \phi(v_i)$.

Initial Height Vector. At the initial stage, we scale and transform a point set Y to ensure they are contained in Ω, and then compute the Voronoi diagram with zero power weights, or namely, with initial heights $h_i = -1/2\|y_i\|^2$, where $\|y_i\|^2$ is the point position in the planar domain. This guarantees that all the cells are non-empty.

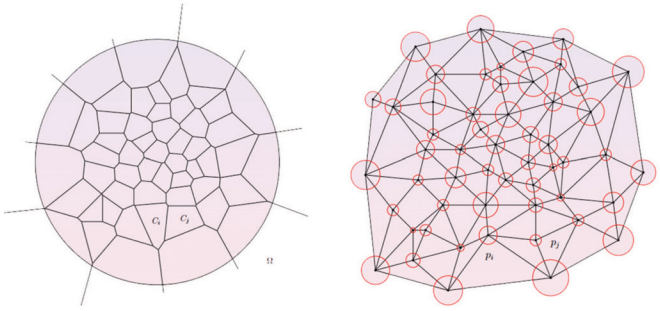

(a) (b)

Fig. 4. Construction of (a) the power Voronoi diagram and (b) the power Delaunay triangulation.

Power Diagram. The OMT based area-preservation computation for the partition of Ω is equivalent to the classical power diagram in computational geometry [11]. Given a point set $Y = \{y_1, y_2, \cdots, y_n\}$, each point y_i associated with the weight w_i as its power, the power distance from any point x to y_i is defined as:

$$Pow(x, y_i) = \frac{1}{2}\|x - y_i\|^2 - \frac{1}{2}w_i,$$

Then, the power diagram is the Voronoi diagram when we use the power distance instead of the standard Euclidean distance.

In our method, the partition induced by the convex function $u_{\mathbf{h}}$ in Eqn. 3 is equivalent to the power diagram with the power weight:

$$w_i = 2h_i + \langle y_i, y_i \rangle.$$

Therefore, the computation can be carried out using power diagram functionalities in standard computational geometry library, such as CGAL [1]. The construction of the power Voronoi diagram and the power Delaunay triangulation are illustrated in Fig. 4.

Hessian Matrix. In our algorithm, we represent the gradient of energy $\nabla E(\mathbf{h})$ in Eqn. 9 as the area changes of cell $(\bar{\mathbf{w}}-\mathbf{w})$, where $\bar{\mathbf{w}}$ and $\mathbf{w}$ as weighting values. Then, compute the dual triangulation and the cell areas to form the gradient, as in Eqn. 9,

$$\nabla E(\mathbf{h}) = (Area(W_i(\mathbf{h}) \cap \Omega))$$

Following the theory proposed by Gu et al. [11], in order to form the Hessian as in Eqn. 10, we compute all edge lengths e_{ij} and the dual edge lengths $\bar{e}_{ij}$ from the power diagram and its dual triangulation (Fig. 4). Then, we use the following matrix: $H(\mathbf{h}) = (h_{ij}(\mathbf{h}))$, where

$$h_{ij}(\mathbf{h}) = \begin{cases} -|e_{ij}|/|\bar{e}_{ij}| & i \neq j, W_i \cap W_j \cap \Omega \neq \emptyset \\ -\sum_{k \neq i} h_{ik} & i = j \\ 0 & otherwise, \end{cases}$$

h_{ij} is the (i, j) entry of a matrix, $(i \neq j)$ is the off diagonal entry, and the diagonal entry is defined as $h_{ii} = -\sum_{k \neq i} h_{ik}$ (namely, h_{ii} is equal to the sum of all off diagonal entries).

Then, we use Newton's method to update the height vector

$$\mathbf{h} \leftarrow \mathbf{h} + \varepsilon H(\mathbf{h})^{-1} \nabla E(\mathbf{h}),$$

where ε is the step length.

Step Length Control. During the computation, it is crucial to ensure that all the cells $W_i(\mathbf{h}) \cap \Omega$ are non-empty. Suppose at step k all the cells are non-empty, then, we update $\mathbf{h_k} \leftarrow \mathbf{h_k} + \varepsilon H(\mathbf{h}_k)^{-1} \nabla E(\mathbf{h_k})$. If some cells are empty in the power diagram induced by $\mathbf{h}_{k+1}$, we will return to $\mathbf{h}_l$, shrink the step length ε to be $1/2\varepsilon$, and try again. If some cells are still degenerated, we shrink the step length iteratively, until all the power cells are non-empty.

Following the implementation details listed in Alg. 1, we have tested our algorithms on different surface models (details in Section 5). For practical implementations, we may need to deal with surface models with different topologies, such as the earth and brain models which are genus zero without any boundary, and map and graph cases which are genus zero with an open boundary. The basic idea is to make the topologies of the source domain and the parameter domain consistent. For example, if we want to map a genus zero surface without an open boundary, such as the brain surface, to a unit disk parameter domain, we cut a very small hole on the surface to get an open boundary so that the source domain and parameter domain have the consistent topology.

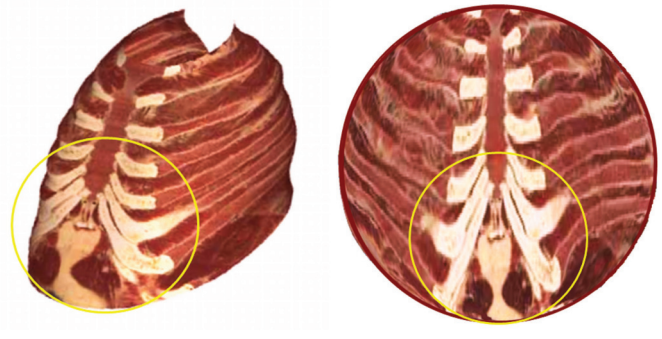

(a) (b)

Fig. 5. Surface flattening of a chest model using our area-preservation mapping for direct display and accurate measurement. The yellow circles highlight the corresponding ROIs between (a) the 3D surface model and (b) the 2D flattened plane.

4.3 ROIs Guided Texture Mapping

After computing the bijective area-preservation surface mapping between the 3D surface model and the flattened 2D disk or rectangular parameter domain, the texture mapping is straightforward with the ROIs guided alignment. With respect to user predefined mapping criteria (e.g., fix the disk boundary or fix the four corner points of a rectangular domain with the alignment of ROIs), the bijective texture mapping between parameterizations and image pixels is syntactically and semantically trivial. We directly call texture mapping functions provided by OpenGL with bilinear interpolation, which is fast and easy to implement. Moreover, we consider model shape and rendering factors, such as depth, view angle, and camera position to obtain reality style visualization, especially for medical data. The pixel color and alpha can be adjusted by the user defined transfer functions.

5 Area-preservation Mapping Applications

To demonstrate the merits of our area-preservation mapping method, we apply our framework to various visualization applications, including the medical and informatics visualization. Then we provide a distortion measurement analysis to demonstrate the advantage of our system in a quantitative fashion.

5.1 Medical Applications

We first test our method using various medical data. Our highly area-preservation results can be obtained in an interactive-rate, even for various large and complicated datasets. For every medical dataset acquired from CT or MRI, we start from using the visualization toolkit (VTK) [17] to convert a volume dataset to a triangulation mesh as the input, with filters to remove noise and aliasing. Then, we can utilize our mapping framework to achieve various visualization results.

Easy and Accurate Area Measurement. Fig. 5 shows a major advantage of our area-preservation mapping and flattening method. Our mapping framework can bijectively project the 3D surface model to a unit 2D disk, so that the physician can directly and accurately visualize and measure the size of the entire ROI area without repeatedly rotating and scaling.

Saliency Feature Guided Area-preservation Mapping. We use saliency map [18] guided area-preservation mapping for diverse computer aided detection (CAD) applications. Fig. 6 shows the design detail. After extracting the surface model (Fig. 6a) from CT colon data (Fig. 6b), we use saliency map [18] for the polyp detection (Fig. 6d). Our area-preservation flattening framework is only applied in the detected ROIs, providing an area-preservation view of polyps for the accurate measurement of the diameter and the size of area (verified by the doctor's measurement as ground truth in the original 3D surface model). By comparison with the conformal mapping method (Fig. 6f), our framework (Fig. 6e) preserves major shape characteristics of the colon surface (e.g., colon folds) without any obviously visual distortion.

Arbitrary Area Weighting Scheme. Flattening the brain surface with area preservation is important to visualize and study neural activity or to detect diseases/disfunctions [38]. For the easy recognition of different brain folds, we use colors to mark different folds as the ROIs (Fig. 1a and Fig. 1b). In contrast to the conformal mapping result (Fig. 1c), Fig. 1d shows our area-preservation mapping result using the MRI brain dataset, which accurately displays accurate sizes of brain folds without severely compressing or stretching. Moreover, users can set different weight coefficients in ROIs to flexibly adjust sizes of different ROI areas (default 1X: equal area).

5.2 Informatics Applications

With the general application property of parameterization and texture mapping, we can easily apply our framework for various informatics applications including earth map, city map and graph.

Earth Map. The fundamental challenge for earth visualization lies at mapping the sphere earth model to a planar domain with maximal information preserved. Direct projection only projects the half sphere, and then causes severe information lost (Fig. 7b). The state-of-the-art method, such as conformal mapping (Fig. 7c), preserves the

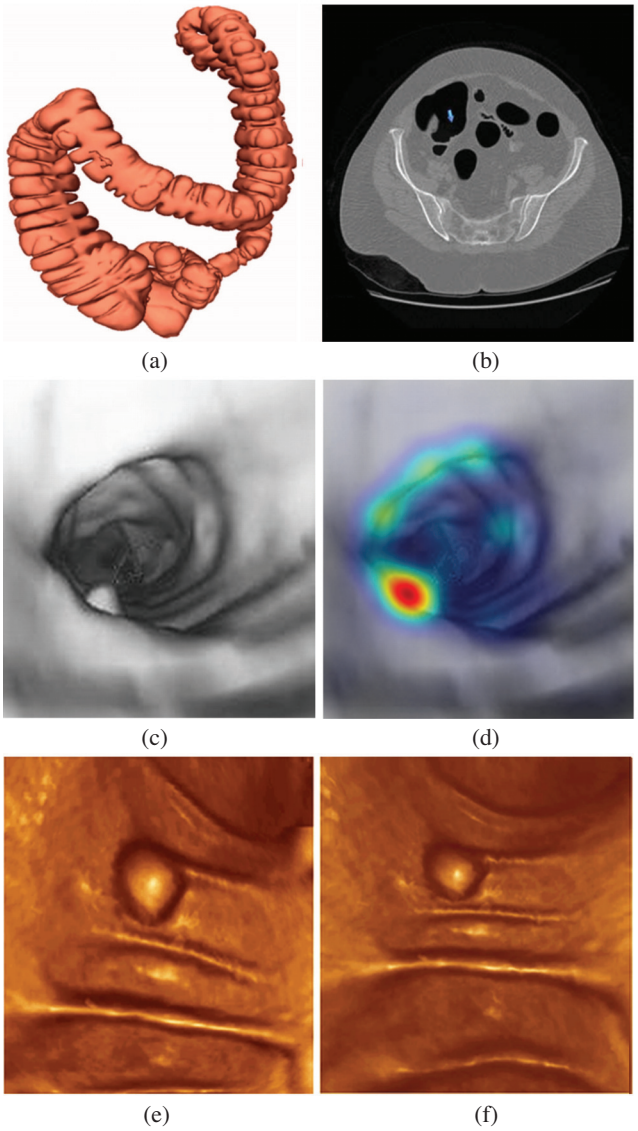

Fig. 6. Saliency map guided area-preservation mapping using a colon model. (a) A 3D colon surface, extracted from CT axis images, such as (b). (c) One possible polyp detected using (d) the saliency map [18]. Surface flattening results using (e) our area-preservation mapping and (f) conformal mapping. By comparison, our result generates the accurate polyp size for area measurement (verified by the doctor's measurement of the polyp as ground truth) without any severe angle distortion.

whole sphere with angle preservation, but severely compresses some continents while inappropriately enlarging others without any control. By comparison, our method (Fig. 7d) can keep the original areas for all major continents, providing the accurate size and area impression for users.

City Map. Our system also provides a direct multiresolution display, functioned as a "magic-lens" to reveal additional details in the ROIs. Our method makes the multiscale alignment accurate but easy without the need of any predefined landmark, due to the accurate area preservation. As shown in Fig. 8, our method generates multiresolution texture mapping to reveal additional street information of the city map. The result demonstrates that our method can well magnify the ROI without causing any obvious distortion.

Network Graph. Our system can generate various visual displays for the graph visualization to satisfy diverse user requirements, due to the flexible weight settings. We showcase its merit using a network visualization example from the AT&T graph library [2], as

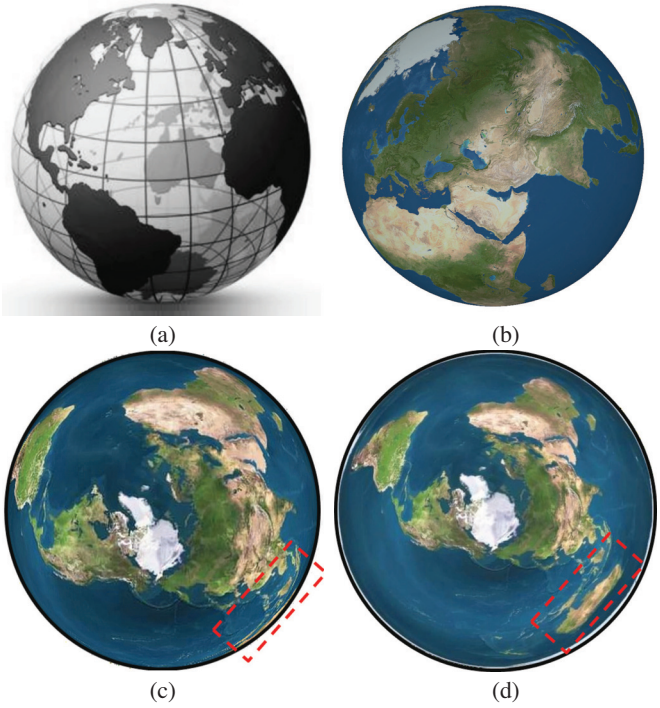

Fig. 7. Different mapping results and comparisons using an earth surface model. (a) A 3D earth model. (b) Direct projection mapping with large information loss. (c) Conformal mapping result with large area distortions. (d) Our area-preservation mapping result with accurate area preservation and small angle distortion (highlighted by the red frames).

shown in Fig. 9a. Each graph node stands for a network station, while each straight line depicts direct connection between two neighbor nodes. Fig. 9b enlarges the radius of the central core to increase the node separation, while compressing exterior nodes to further reduce the potential attention. Fig. 9c shows another area manipulation style: compressing central nodes while enlarging exterior nodes for further separation. There is no efficient way to generate a similar result using either geometry methods (e.g., conformal magnifier [33]) or deformation methods (e.g., moving least squares [31, 32]). Taking a close look at Fig. 9d, the conformal magnifier fails to flexibly control magnification ratios in both focus and context regions. It excessively enlarges the central core area, while compressing exterior nodes without any control. By comparison, our system can easily manipulate the size of area everywhere to generate user preferred views with appropriate node distributions.

Hierarchical Magnification. We can directly apply our mapping framework as a cascaded magnifier: applying the same magnifier repeatedly on the prior computing magnification result to obtain exponentially increasing magnification ratios. Since our method can accurately preserve the size of area by setting the target weight, we can guarantee that the final target region would be precise after each magnification process. Fig. 10 shows that our hierarchical magnification can easily and accurately reach the high magnification ratio.

5.3 Implementation

In order to support fast visual display, our framework combines both CPU and GPU for computing optimization, parameterization, texture mapping and volume rendering using C++ with OpenGL library. Our algorithm and solution of the optimal transport map is easy to implement robustly to have interactive-rate computation for most experimental cases in this paper, overcoming a major limitation of the OMT problem - computation inefficiency. By comparison with other optimization algorithms, such as [10] and [37], comparative experiments show that our system provides a significant speedup, empirically at least 3-5 times faster, as shown in Table 1 (more comparison details are listed in Section 2). For the application of large volumetric data

Fig. 8. Multiresolution view without any predefined landmarks. (a) The original New York city (NYC) map. (b) NYC map with multiresolution texture images. The red frames highlight the corresponding multiresolution texture maps in the ROI. (c) Area manipulation result with a detailed view to show additional street information. The high resolution detail view can be easily aligned/merged into the low scale map without using any landmark due to accurate area preservation.

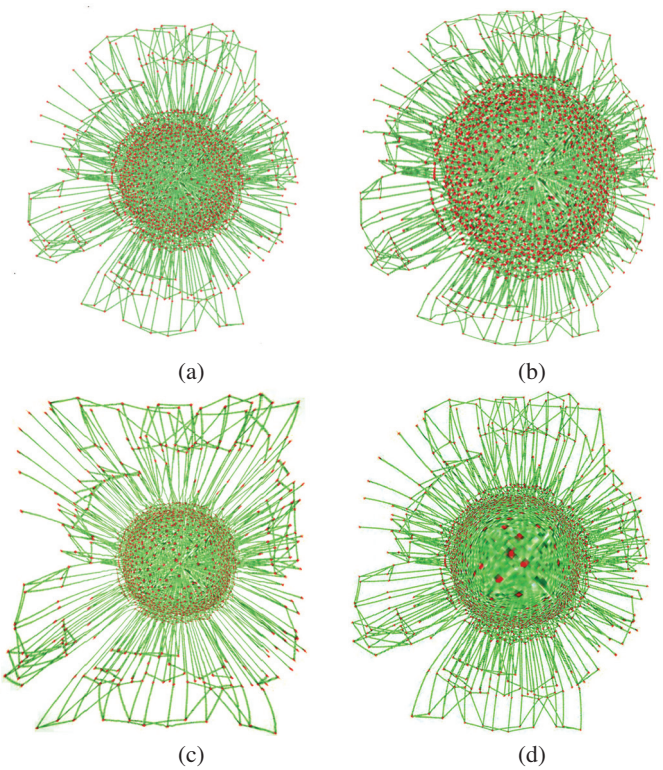

Fig. 9. Mapping comparisons using the network graph. (a) Original graph layout [2]. Magnification results with (b) the central nodes as the ROI, and with (c) the surrounding exterior nodes as the ROI, using our framework. (d) Magnification result using conformal magnifier [33]. By comparison, our method has flexible area control to generate various views.

(e.g., brain dataset with size $256^2 \times 142$), we can easily obtain full resolution results in interactive-rate using various surface models with texture mapping or volume rendering. To further increase the flexibility of system control, our framework embeds mesh editing tools, allowing users to interactively choose a tradeoff between quality and computing speed.

All experiments have been carried out on an Intel Core2Duo 2.2GHz laptop with 4GB memory and Windows 7 as the operating system. Generally, the cost linearly depends on the property of the surface models (the vertex and face counts) and the number of iterations needed for the desired accuracy. Table 2 presents detailed performance of our method, which shows that our method is significantly fast and suitable for real-time/interactive operations, even for large datasets with high resolution requirements. In theory, finer surface models increase in resolution to support finer rendering but having longer computation time. Fortunately, the combination of saliency map and hierarchical mesh design (high resolution in the ROI, while low resolution in the context) allows our framework to work accurately and effectively.

Table 1. Performance comparison of several area-preservation methods (e.g., Dominitz et al. [10] and Zou et al. [37]) using models with different vertex and face counts. N: the number of vertices, F: the number of faces, AP: area-preservation parametrization time (in ms).

Model	N	F	Our AP	AP [10]	AP [37]
Tube	1649	3035	102	278	951
HemiSphere	3456	6846	265	815	2436
Square	5252	10471	474	1926	7104
Gaussian	10201	20006	812	5142	15705

Table 2. Computing time for all experimental cases using our framework. N: the number of vertices, F: the number of faces, AP: area-preservation parametrization time (bijective mapping) and T: texture mapping time.

Model	Texture	N	F	AP (ms)	T (ms)
Chest	Chest	1528	2999	97	42
Brain	MRI brain	14499	29662	1254	108
Colon	CT colon	12762	24953	1096	97
Sphere	Earth	3456	6846	265	63
Square	City	5252	10471	474	62
Sphere	Graph	3456	6846	265	71
Gaussian	Graph	10201	20006	812	45

5.4 Quantitative Analysis for Area-preservation Mapping

The main challenge of a good area-preservation mapping is yielding strict equality of area elements between the original surface and the flattened result at its final state. We examine both the area distortion and the quasi-conformal distortion per face over the mesh as the quantitative analysis. We define γ_{max} and γ_{min} as the larger and smaller eigenvalues of the Jacobian of the affine transformation that maps the domain triangles to the original surface, normalized with the hypothesis that the total area of the surface equals that of the domain. Then, the area distortion metric Υ is computed as $\Upsilon = log(\gamma_{max}\gamma_{min})$, while the quasi-conformal distortion metric Λ is computed using $\Lambda = log(\frac{\gamma_{max}}{\gamma_{min}})$. In both cases, zero indicates that there is no distortion and a larger

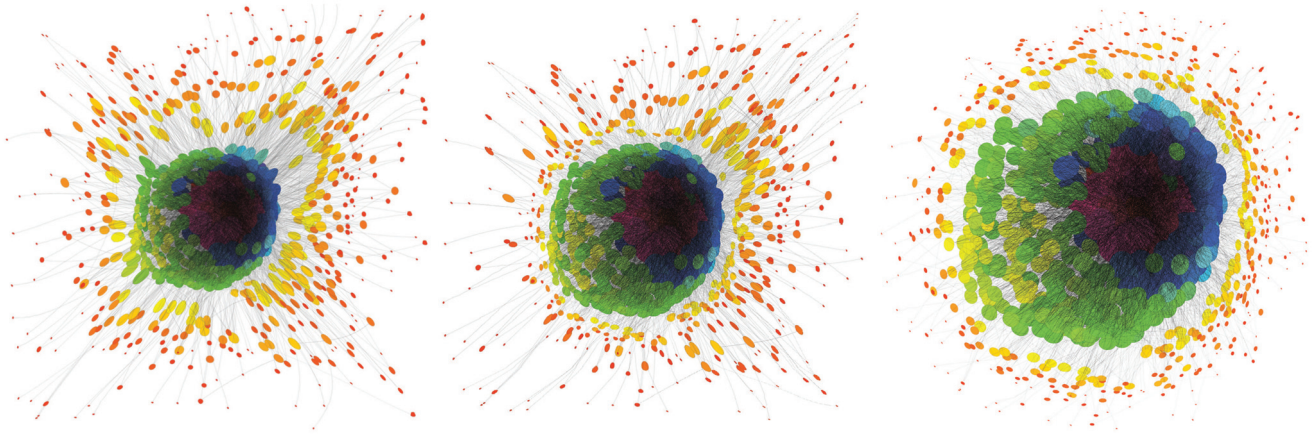

(a) (b) (c)

Fig. 10. Hierarchical magnification views of a simulated radial graph. Colors are used to illustrate the node overlaps: from red (no overlap) to purple (most overlap). (a) Original radial graph. (b) 2X and (c) 4X cascade magnification results. The 4X magnification is generated using the 2X magnifier again on its prior magnified result. With the increasing magnification ratio, the central nodes are enlarged for a clear separation view, while compressing the exterior nodes.

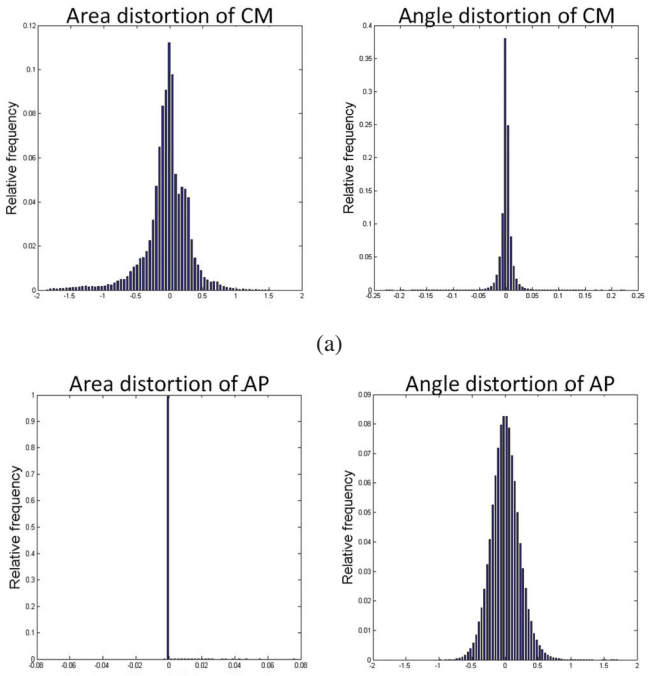

Fig. 11. Comparison histograms of mapping distortions using the lion head model of Fig. 2. (a) Conformal mapping (CM) and (b) our area-preservation mapping (AP). Left column: the area distortion. Right column: the angle distortion. By comparison, our framework (b) generates good mapping results with accurate area preservation and small angle distortions.

value means a larger distortion.

Fig. 11 shows the histograms of the area distortion and the quasi-conformal (angle) distortion for both conformal mapping [29] and our area-preservation approach, using the lion head surface model (Fig. 2). By comparison with conformal mapping, as shown in Fig. 11b, our system can generate good area-preservation results with very small area distortions (the area-distortion error distribution is less than 2%) even for the complicated surface model (in theory, more complicated models typically lead to larger area distortion errors). Therefore, our framework has accurately linear area magnification with respect to predefined weighting values.

6 Conclusions and Future Work

In this paper, we present a new framework using the optimal mass transport method, which is implemented in a novel manner and used for various visualization and graphic applications. We present a computationally efficient numerical scheme to achieve the area-preservation mapping. With the combination of CPU and GPU, our system becomes practical for the use on large 3D datasets in terms of both speed and accuracy. Our system is built based on geometric parameterization techniques, where an area-preservation map with the minimal area distortion is generated for each input 3D surface model. The use of parameterization is compatible with various volume applications, easily and efficiently supporting the handling of various complicated data [20]. Moreover, the saliency map makes it easy and accurate to detect arbitrary ROIs and further supports mesh reduction in the context area. With respect to selected ROIs, results are generated after texture mapping or volume rendering using corresponding parameterized surface models to obtain flattened views with the optimized area preservation. In term of interactive operations, users can simply set different weights in the ROIs, enabling an extremely flexible style of area manipulations for data exploration and analysis. All experimental results and comparisons have demonstrated that our new OMT bases optimization approach has great potentials and applications in visualization and graphics.

A major limitation of our framework is that due to the mapping theory, our system inevitably generates angle distortions for achieving optimal area-preservation mapping. However, because we embed conformal mapping into our system (initialization), users can interactively select mapping styles to satisfy various requirements. For the future work, inspired by Sandhu et al. [26] and Wang et al. [28], our framework can be further extended to volumetric mapping. Meanwhile, because we use Voronoi diagram and its dual Delaunay triangulation for our OMT based mapping, inspired by Rong et al. [24], we can use the GPU to further accelerate the computing speed. In addition, a formal user study is necessary to further demonstrate advantages of our framework for various applications.

Acknowledgment

This work has been supported by NSF grants IIS-0916235, CNS-0959979, IIP-1069147, DMS-1221339, NETS-1016829, III-0916286, CCF-1081424 and CCF-0830550. The authors would also like to thank Stony Brook University Hospital for providing the medical data.

REFERENCES

[1] CGAL, Computational Geometry Algorithms Library. http://www.cgal.org.

[2] AT&T graph library. *http://www.graphdrawing.org*, 2009.

[3] A. D. Alexandrov. Convex polyhedra. *Springer Monographs in Mathematics*. *Springer-Verlag, Berlin*, 2005.

[4] F. Aurenhammer. Power diagrams: properties, algorithms and applications. *SIAM Journal of Computing*, 16(1):78–96, 1987.

[5] N. Bonneel, M. van de Panne, S. Paris, and W. Heidrich. Displacement interpolation using Lagrangian mass transport. *ACM Trans. Graph. (SIGGRAPH Asia)*, 30:158:1–158:12, 2011.

[6] N. Bonnotte. From Knothe's rearrangement to Brenier's optimal transport map. *arXiv:1205.1099 [math.OC]*, pages 1–29, 2012.

[7] Y. Brenier. Polar factorization and monotone rearrangement of vector-valued functions. *Comm. Pure. Appl. Math.*, 44(4):375–417, 1991.

[8] F. de Goes, K. Breeden, V. Ostromoukhov, and M. Desbrun. Blue noise through optimal transport. *ACM Trans. Graph. (SIGGRAPH Asia)*, 31:1–10, 2012.

[9] F. de Goes adn D.Cohen-Steiner, P. Alliez, and M. Desbrun. An optimal transport approach to robust reconstruction and simplification of 2D shapes. *Eurographics Symposium on Geometry Processing*, 30(5):1593–1602, 2011.

[10] A. Dominitz and A. Tannenbaum. Texture mapping via optimal mass transport. *IEEE Transactions on Visualization and Computer Graphics*, 16(13):419–432, 2010.

[11] X. Gu, F. Luo, J. Sun, and S.-T. Yau. Variational principles for Minkowski type problems, discrete optimal transport, and discrete Monge-Ampere equations. *arXiv:1302.5472 [math.GT]*, pages 1–13, 2013.

[12] X. Gu, Y. Wang, T. Chan, P. Thompson, and S.-T. Yau. Genus zero surface conformal mapping and its application to brain surface mapping. *IEEE Transactions on Medical Imaging*, 23(8):949–958, 2004.

[13] S. Haker, S. Angenent, A. Tannenbaum, and R. Kikinis. Nondistorting flattening maps and the 3D visualization of colon CT images. *IEEE Trans. Med. Imag.*, 19(7):665–670, 2000.

[14] S. Haker, L. Zhu, A. Tannenbaum, and S. Angenent. Optimal mass transport for registration and warping. *International Journal on Computer Vision*, 60:225–240, 2004.

[15] S. Halier, S. Angenent, A. Tannenbaum, and R. Kikinis. Nondistorting flattening maps and the 3D visualization of colon CT images. *IEEE Transactions on Medical Imaging*, 19(7):665–670, 2000.

[16] L. Kantorovich. On a problem of Monge. *Uspekhi Mat. Nauk.*, 3:225–226, 1948.

[17] Kitware, Inc. *The Visualization Toolkit User's Guide*, January 2003.

[18] C. Koch and S. Ullman. Shifts in selective visual attention: towards the underlying neural circuitry. *Human Neurobiology*, (4):219–227, 1985.

[19] B. Li, X. Li, K. Wang, and H. Qin. Surface mesh to volumetric spline conversion with generalized poly-cubes. *IEEE Transactions on Visualization and Computer Graphics*, Preprint, 2013.

[20] B. Li and H. Qin. Feature-aware reconstruction of volume data via trivariate splines. *Pacific Graphics*, pages 49–54, 2011.

[21] Q. Merigot. A multiscale approach to optimal transport. *Comput. Graph. Forum*, 30(5):1583–1592, 2011.

[22] G. Monge. Mémoire sur la théorie des déblais et de remblais. *Histoire de l'Académie Royale des Sciences de Paris, avec les Mémoires de Mathématique et de Physique pour la meme année,*, pages 666–704, 1781.

[23] S. Rachev and L. Ruschendorf. *Mass Transportation Problems*, volume I-II. Springer, New York, 1998.

[24] G. Rong, Y. Liu, W. Wang, X. Yin, X. Gu, and X. Guo. GPU-assisted computation of centroidal Voronoi tessellation. *IEEE Transactions on Visualization and Computer Graphics*, 17(3):345–356, 2011.

[25] Y. Rubner, C. Tomasi, and L. J. Guibas. The earth mover's distance as a metric for image retrieval. *International Journal of Computer Vision*, 40:99–121, 2000.

[26] R. Sandhu, A. Dominitz, Y. Gao, and A. Tannenbaum. Volumetric mapping of genus zero objects via mass preservation. *CoRR*, abs/1205.1225:1–12, 2012.

[27] T.Rehman, E.Haber, G.Pryor, J.Melonakos, and A.Tannenbaum. 3D nonrigid registration via optimal mass transport on the GPU. *Medical Image Analysis*, 13:931–40, 2009.

[28] K. Wang, X. Li, B. Li, H. Xu, and H. Qing. Restricted trivariate polycube splines for volumetric data modeling. *IEEE Transactions on Visualization and Computer Graphics*, 18(5):703–716, 2012.

[29] Y. Wang, J. Shi, X. Yin, X. Gu, T. F. Chan, S. T. Yau, A. W. Toga, and P. M. Thompson. Brain surface conformal parameterization with the Ricci flow. *IEEE Trans. Med. Imag.*, 31(2):251–264, Feb 2012.

[30] W. Zeng, J. Marino, A. E. Kaufman, and X. D. Gu. Volumetric colon wall unfolding using harmonic differentials. *Computers and Graphics*, 35(3):726—-732, 2011.

[31] X. Zhao, B. Li, L. Wang, and A. Kaufman. Focus+context volumetric visualization using 3D texture-guided moving least squares. *Computer Graphics International*, pages 17–25, 2011.

[32] X. Zhao, B. Li, L. Wang, and A. Kaufman. Texture-guided volumetric deformation and visualization using 3D moving least squares. *The Visual Computer*, 28:193–204, 2012.

[33] X. Zhao, W. Zeng, X. D. Gu, A. E. Kaufman, W. Xu, and K. Mueller. Conformal magnifier: A focus+context technique with local shape preservation. *IEEE Transactions on Visualization and Computer Graphics*, 18(11):1928–1941, 2012.

[34] L. Zhu, S. Haker, and A. Tannenbaum. Flattening maps for the visualization of multibranched vessels. *IEEE Trans. Med. Imag.*, 24(2):191–198, 2005.

[35] L. Zhu, Y. Yang, S. Haker, and A. Tannenbaum. An image morphing technique based on optimal mass preserving mapping. *IEEE Trans. Med. Imag.*, 16(6):1481–1495, 2007.

[36] G. Zigelman, R. Kimmel, and N. Kiryati. Texture mapping using surface flattening via multidimensional scaling. *IEEE Transactions on Visualization and Computer Graphics*, 8(2):198–207, 2002.

[37] G. Zou, J. Hu, X. Gu, and J. Hua. Area-preserving surface flattening using Lie advection. *Medical Image Computing and Computer-Assisted Intervention (MICCAI)*, 14:335–342, 2011.

[38] G. Zou, J. Hu, X. Gu, and J. Hua. Authalic parameterization of general surfaces using Lie advection. *IEEE Transactions on Visualization Computer Graphics*, 17(12):2005–2014, 2011.